

SIMULTANEOUS TRANSVERSE OSCILLATIONS OF A PROMINENCE AND A FILAMENT AND LONGITUDINAL OSCILLATION OF ANOTHER FILAMENT INDUCED BY A SINGLE SHOCK WAVE

YUANDENG SHEN^{1,2,3,4}, YING D. LIU², P. F. CHEN⁴, AND KIYOSHI ICHIMOTO³

¹ Yunnan Observatories, Chinese Academy of Sciences, Kunming 650011, China; ydshen@ynao.ac.cn

² State Key Laboratory of Space Weather, Chinese Academy of Sciences, Beijing 100190, China

³ Kwasan and Hida Observatories, Kyoto University, Yamashina-ku, Kyoto 607-8471, Japan

⁴ Key Laboratory of Modern Astronomy and Astrophysics, School of Astronomy & Space Science, Nanjing University, Nanjing 210093, China

Received 2014 April 24; accepted 2014 September 3; published 2014 October 22

ABSTRACT

We present the first stereoscopic and Doppler observations of simultaneous transverse oscillations of a prominence and a filament and longitudinal oscillation of another filament launched by a single shock wave. Using $H\alpha$ Doppler observations, we derive the three-dimensional oscillation velocities at different heights along the prominence axis. The results indicate that the prominence has a larger oscillation amplitude and damping time at higher altitude, but the periods at different heights are the same (i.e., 13.5 minutes). This suggests that the prominence oscillates like a linear vertical rigid body with one end anchored on the Sun. One of the filaments shows weak transverse oscillation after the passing of the shock, which is possibly due to the low altitude of the filament and the weakening (due to reflection) of the shock wave before the interaction. Large-amplitude longitudinal oscillation is observed in the other filament after the passing of the shock wave. The velocity amplitude and period are about 26.8 km s^{-1} and 80.3 minutes, respectively. We propose that the orientation of a filament or prominence relative to the normal vector of the incoming shock should be an important factor for launching transverse or longitudinal filament oscillations. In addition, the restoring forces of the transverse prominence are most likely due to the coupling of gravity and magnetic tension of the supporting magnetic field, while that for the longitudinal filament oscillation is probably the resultant force of gravity and magnetic pressure.

Key words: Sun: activity – Sun: filaments, prominences – Sun: flares – Sun: magnetic fields – Sun: oscillations

Online-only material: animations, color figures

1. INTRODUCTION

Solar prominences, or filaments, are cool and dense plasmas supported by coronal magnetic fields, and their eruption often causes large-scale reconfiguration of coronal magnetic fields and is usually the source of solar storms that can influence near-Earth space environmental conditions (e.g., Chen 2011; Fang 2012; Shen et al. 2012; Wang & Ji 2013; Liu et al. 2014). For the past several decades, the dynamics of solar prominences has been the subject of a large number of studies. However, many fundamental problems regarding prominences are still open questions (Shen et al. 2011, 2012d, 2012e; Bi et al. 2012, 2013; Parenti 2014). Therefore, the investigation of the basic physics in prominences is of particular importance in solar physics. In this paper, we focus on the intriguing large-amplitude oscillatory motion in prominences/filaments, which is rarely observed; many questions about this phenomenon are yet to be understood (Tripathi et al. 2009). On the other hand, many studies have indicated that small-amplitude oscillations in prominences are a common phenomenon, and are thought to be locally generated by perturbations omnipresent in the photosphere and chromosphere (Arregui et al. 2012). Prominences and filaments are the same entities, with the former seen in emission over the solar limb and the latter on the disk in absorption. We will use the two terms interchangeably throughout the paper.

Large-amplitude oscillatory motion in prominences has been observed for about 80 years, since the early reports in the 1930s (Dyson 1930; Newton 1935). Previous observations have indicated that oscillating filaments are in tight association with remote flare activities and global shock waves (Moreton & Ramsey 1960; Shen & Liu 2012b, 2012c; Shen et al. 2013a;

Yang et al. 2013; Xue et al. 2013; Liu & Ofman 2014). Due to the interaction with shock waves, a filament usually starts to oscillate with a large downward motion and then experiences an up-and-down damping harmonic oscillation process (Dodson 1949; Bruzek 1951; Moreton & Ramsey 1960; Shen et al. 2014; Xue et al. 2014). If one observes an oscillating filament using $H\alpha$ line wings, the filament will periodically appear and disappear in the line wing due to the Doppler effect. Therefore, this kind of oscillating filament historically has also been called “winking filaments.” Ramsey & Smith (1966) studied 11 winking filaments and found that filaments always oscillate with their own characteristic frequency, which is determined by an inherent property of the filament rather than the disturbance agents. Previous studies have indicated that winking filaments are usually initiated by fast magnetohydrodynamic (MHD) shocks in the solar atmosphere, for example, chromosphere Moreton waves (Moreton & Ramsey 1960) and coronal EUV waves (Shen & Liu 2012b; Shen et al. 2014). Since the speed of a fast MHD wave is faster in the corona than that in the chromosphere, the normal vector of the wavefront points downward as the wave travels from the flare site (Uchida 1968; Liu et al. 2012, 2013). Therefore, the arrival of a shock wave will push the filament downward to a certain displacement at first, and then it will oscillate for a few cycles with a coupling of gravity and magnetic forces as a restoring force. According to the classification of large-amplitude filament oscillations, the winking filaments belong to transverse and/or vertical filament oscillations, whose oscillation direction is perpendicular to the filament’s main axis. In many studies, the chromosphere Moreton wave is often thought of as the trigger of winking filaments (Eto et al. 2002). However, coronal EUV

waves could also trigger the oscillations of some filaments (Okamoto et al. 2004; Kumar et al. 2013; Shen et al. 2014) and coronal loops (Shen & Liu 2012b; Kumar et al. 2013; Zheng et al. 2013). Very recently, Shen et al. (2014) observed a chain of winking filaments in association with a remote flare and a bright EUV wave in the west hemisphere. In this event, there is no chromosphere Moreton wave that could be detected in $H\alpha$ observations, and the EUV wave is also difficult to identify at the location of a long filament in the east hemisphere. The authors found that the initiation of the filament oscillation is in agreement with the inferred arrival time of the lateral surface EUV wave, which is driven by the associated coronal mass ejection (CME) at first and then freely propagates in the corona along the solar surface. This observation suggests that some winking filaments can be triggered by invisible (weak) shock waves. According to the table in Tripathi et al. (2009) and Shen et al. (2014), the velocity amplitude, period, and damping time of winking filaments are in the ranges of 6–41 km s^{-1} , 11–29, and 25–180 minutes, respectively. Theoretical investigations of transverse/vertical filament oscillations have also been performed by Hyder (1966) and Kleczek & Kuperus (1969), in which the magnetic tension is considered the main restoring force, while the damping can be attributed either to energy loss through the emission of shock waves into the ambient corona or to various dissipative processes (Tripathi et al. 2009 and references therein).

Besides large-amplitude transverse filament oscillations, Jing et al. (2003) first reported another type of large-amplitude oscillation in filaments, i.e., longitudinal filament oscillation, where the oscillatory motion is along the filament axis. According to previous studies, the velocity amplitude, period, and damping time of longitudinal oscillations are in ranges of 30–100 km s^{-1} , 44–160, and 115–600 minutes, respectively. Previous observations have indicated that the initiation of longitudinal oscillation in filaments is often related to the nearby microflare or jet activities (Jing et al. 2003, 2006; Vrřnak et al. 2007; Li & Zhang 2012; Bi et al. 2014). However, what is the main restoring force is still an open question. Generally speaking, there are three candidate forces that could be the restoring force for longitudinal filament oscillations, i.e., gravity, magnetic pressure, and magnetic tension forces. Vrřnak et al. (2007) explained the trigger of longitudinal filament oscillations in terms of poloidal magnetic flux injection into the filament by magnetic reconnection at one of the filament legs, and the magnetic pressure gradient along the filament axis is proposed to be the restoring force. However, Li & Zhang (2012) suggested that the restoring force is probably the coupling of the magnetic tension and gravity. Theoretical works have also been performed to investigate the restoring force and damping mechanisms of large-amplitude longitudinal filament oscillations (Luna et al. 2012, 2014; Luna & Karpen 2012; Zhang et al. 2012, 2013). The authors found that the main restoring force is mainly the projection component of the gravity along the filament axis, while the damping is possibly related to the wave leakage, mass accretion, and geometry of the magnetic structure that supports the filament mass. It should be noted that in these numerical studies the authors did not take the filament magnetic field into account.

In addition to the abovementioned large-amplitude transverse and longitudinal filament oscillations, large-amplitude long and ultra-long-period filament oscillations are also observed (say, 8–27 hr), which is interpreted in terms of slow string MHD modes and/or thermal overstability associated with peculiarities of the cooling/heating function (Foullon et al. 2004, 2009).

On 2012 October 15, the oscillation of a polar crown filament was observed before and during the slow-rising pre-eruption phase, and the period is about 2.5 hr (Isobe & Tripathi 2006; Isobe et al. 2007; Pintér et al. 2008; Chen et al. 2008). The authors proposed that the fast magnetic reconnection that changes the equilibrium of the supporting magnetic system could be the possible trigger mechanism. These observations of prominence oscillations can provide a powerful diagnostic tool for forecasting the prominence eruption. Observation of large-amplitude prominence oscillations is important for studying the properties of prominences and the surrounding coronal plasma with the so-called prominence seismology (e.g., Hyder 1966; Uchida 1970; Isobe et al. 2007; Pintér et al. 2008; Hershaw et al. 2011). In addition, it is also important for diagnosing the characteristics and the arrival of large-scale MHD waves in the solar atmosphere (e.g., Eto et al. 2002; Okamoto et al. 2004; Gilbert et al. 2008; Gosain & Foullon 2012; Jackiewicz & Balasubramaniam 2013; Shen et al. 2014). For more background knowledge on filament oscillations, we refer to several recent reviews (Oliver & Ballester 2002; Tripathi et al. 2009; Arregui et al. 2012).

In this paper, we present the first observations of simultaneous transverse oscillations of a prominence and a filament and longitudinal oscillation of another filament launched by the shock wave in association with the impulsive *GOES* X6.9 flare on 2011 August 9. This flare is so far the most powerful one in the current solar cycle 24, and it has attracted a lot of attention from solar physicists. Shen & Liu (2012c) and Asai et al. (2012) studied the associated shock wave in different layers of the solar atmosphere in which the authors first reported the corresponding wave signature at the bottom layer of the chromosphere, which suggests that a stronger shock wave can reach down deeper into the solar atmosphere. This event also caused the oscillation of a nearby loop system (Srivastava & Goossens 2013), the peculiar phenomenon of microwave quasi-periodic pulsation (Tan & Tan 2012), and influenced the Earth's electrodynamics of the equatorial and low-latitude ionosphere (Sripathi et al. 2013). Although Asai et al. (2012) briefly studied the associated prominence oscillation in this event, here we present a more detailed analysis about the prominence and filament oscillations involved in this event, with Doppler and stereoscopic observations taken by the Solar Magnetic Activity Research Telescope (SMART; Ueno et al. 2004), the *Solar Dynamics Observatory* (*SDO*; Pesnell et al. 2012), and the *Solar TERrestrial RELations Observatory* (*STEREO*; Kaiser et al. 2008). Instruments and data sets are described in Section 2, results are presented in Section 3, and discussions and conclusions are given in Section 4.

2. INSTRUMENTS AND DATA SETS

In this paper, we use stereoscopic and Doppler multi-wavelength observations to study the simultaneous prominence and filament oscillations caused by the global shock wave in association with the X6.9 flare on 2012 August 9. The instruments used include SMART, *SDO*, and *STEREO*-Ahead, and the flare light curves recorded by the *Geostationary Operational Environmental Satellite* (*GOES*) and the *Reuven Ramaty High Energy Solar Spectroscopic Imager* (*RHESSI*; Lin et al. 2002). SMART is a ground-based telescope at Hida Observatory of Kyoto University, Japan that is designed to observe the dynamic chromosphere and the photospheric magnetic field. We use the full-disk $H\alpha$ images taken in seven wavelengths at $H\alpha$ center,

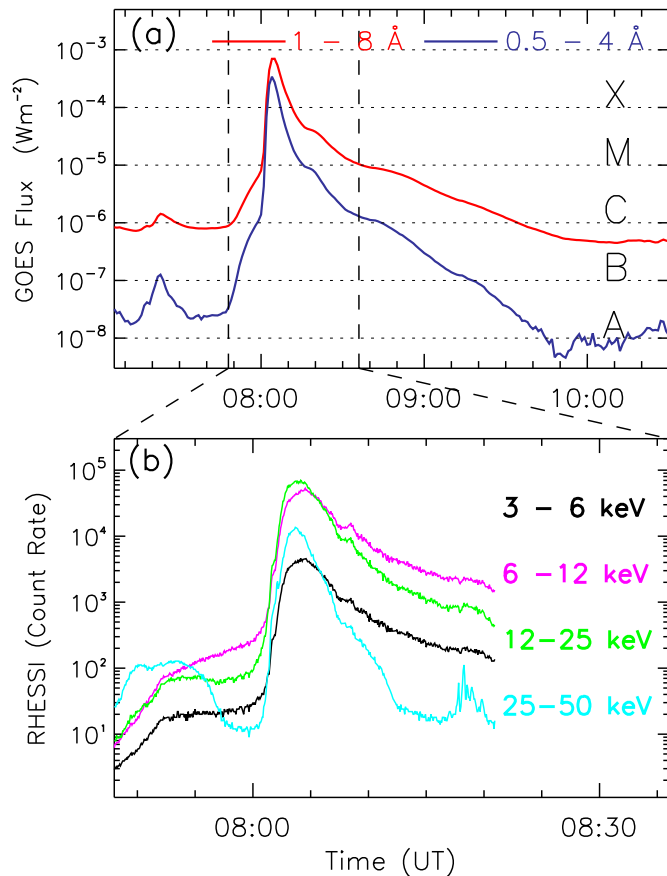


Figure 1. Soft and hard X-ray light curves of the X6.9 flare. The top panel shows the *GOES* soft X-ray profiles of 0.5–4 Å (blue) and 1–8 Å (red), while the bottom one shows the *RHESSI* hard X-ray count rates in the energy bands (4 s integration) of 3–6 keV (black), 6–12 keV (magenta), 12–25 keV (green), and 25–50 keV (cyan). The two vertical dashed lines in the top panel indicate the time interval of the bottom one.

(Animations and a color version of this figure are available in the online journal.)

± 0.5 Å, ± 0.8 Å, and ± 1.2 Å. The telescope takes images with the seven channels nearly simultaneously (< 1 minute), and the field of view (FOV) and pixel resolution are $2300'' \times 2300''$ and $0''.6$, respectively. The cadence of the images is 2 minutes. The high temporal and spatial resolution EUV observations are taken by the Atmospheric Imaging Assembly (AIA; Lemen et al. 2012) on board *SDO*, which provides continuous images at seven EUV and three UV-visible channels, and the cadence and pixel size are 12 s and $0''.6$, respectively. The full-disk EUV observations taken by *STEREO*-Ahead are also used in this paper. On 2011 August 9, the separation angle between *STEREO*-Ahead and the Earth was about 101° . Since the source region is located close to the west limb from the Earth’s view angle, the event was not observed by *STEREO*-Behind. The pixel size of *STEREO* images is $1''.58$, while the cadences of the 195 Å 304 Å and 171 Å images are 5, 10, and 120 minutes, respectively. All images used in this paper are differentially rotated to a reference time of 08:05 UT using the standard SolarSoftWare (SSW), and north is up and east is to the left.

3. RESULTS

3.1. Overview of the Event

Figure 1 shows the soft and hard X-ray light curves of the *GOES* X6.9 flare that occurred in NOAA active region (AR)

11263 (N18W80) on 2011 August 9. The start, peak, and stop times of the flare are 07:48:00, 08:05:00, and 08:08:00 UT, respectively. During the rising phase of the flare, microwave quasi-periodic pulsations with millisecond timescale superfine structures are observed that reflect the micro magnetic reconnection process and the dynamics of energetic electrons in the flaring process (Tan & Tan 2012). Such microwave superfine structures are possibly important for understanding the driving mechanism of the recently discovered quasi-periodic fast propagating magnetosonic waves (Liu et al. 2010, 2011, 2012; Shen & Liu 2012a; Shen et al. 2013b; Yuan et al. 2013). The flare was accompanied by a type II radio burst and a halo CME whose average speed is about 1610 km s^{-1} (Shen & Liu 2012c). This impulsive flare also resulted in the sudden enhancement of total electron content in the sunlit hemisphere and the sudden decrease and increase in the geomagnetic northward (H) component’s strength at the equatorial and low-latitude ionosphere of the Earth (Sripathi et al. 2013). In the low solar atmosphere, an impulsive shock wave is observed simultaneously from the top of the photosphere (say, AIA 1700 Å) to the low corona, and it directly resulted in the oscillation of a prominence and two filaments far from the flare. According to Shen & Liu (2012c), the shock wave propagated with an extremely high speed of 1000 km s^{-1} at the initial stage, but it quickly decelerated to a moderate speed of 605 km s^{-1} . Asai et al. (2012) roughly estimated the oscillation period and amplitude of the prominence, which are about 12–16 minutes and 10 Mm, respectively. Using the Doppler and stereoscopic multi-wavelength high-resolution observations taken by SMART, *SDO*, and *STEREO*-Ahead, in this paper we will present more details about the oscillating prominence and the other two filaments.

An overview of the pre-event magnetic condition around the flare source region is shown in Figure 2. From the Earth’s angle of view, the location of AR11263 is close to the west limb in the northern hemisphere, while a filament (F1) and a prominence (P) can be observed in the southern hemisphere (see Figures 2(a)–(d)). From the *STEREO*-Ahead angle of view, AR11263 and F1 are close to the west limb, while P can be identified as a long filament along the north–south direction. In addition to F1 and P, there is another filament (F2) close to the meridian line in the *STEREO*-Ahead observations (see Figures 2(e)–(g)). Large-amplitude oscillation of the two filaments and the prominence are observed right after the passing of the shock wave. Panels (h) and (i) are AIA 193 Å and *STEREO*-Ahead 195 Å images, respectively. They are overlaid with the three-dimensional coronal fields extrapolated with the potential field source surface software (Schrijver & De Rosa 2003), where the green and white lines represent the calculated open and closed field lines, respectively. One can see that most of the region of interest is covered with a closed field except for a small region between F1 and the prominence, where the dominant magnetic field is open (see the green lines in Figures 2(h) and (i)). With a pair of AIA 193 Å and *STEREO*-Ahead 195 Å images at 07:46:15 UT, the three-dimensional structures of F1 and the prominence can be reconstructed using the procedure “scc_measure.pro” developed by W. Thompson. The results show that the heights of F1 and the prominence are 34.8 ± 1.5 and 79.0 ± 2.7 Mm, respectively. Here, the errors are given by the standard derivation of the measured data. The lower altitude of F1 could be one of the possible reasons accounting for the weak oscillation of F1. The height of F2 cannot be obtained because observations are only available from *STEREO*-Ahead.

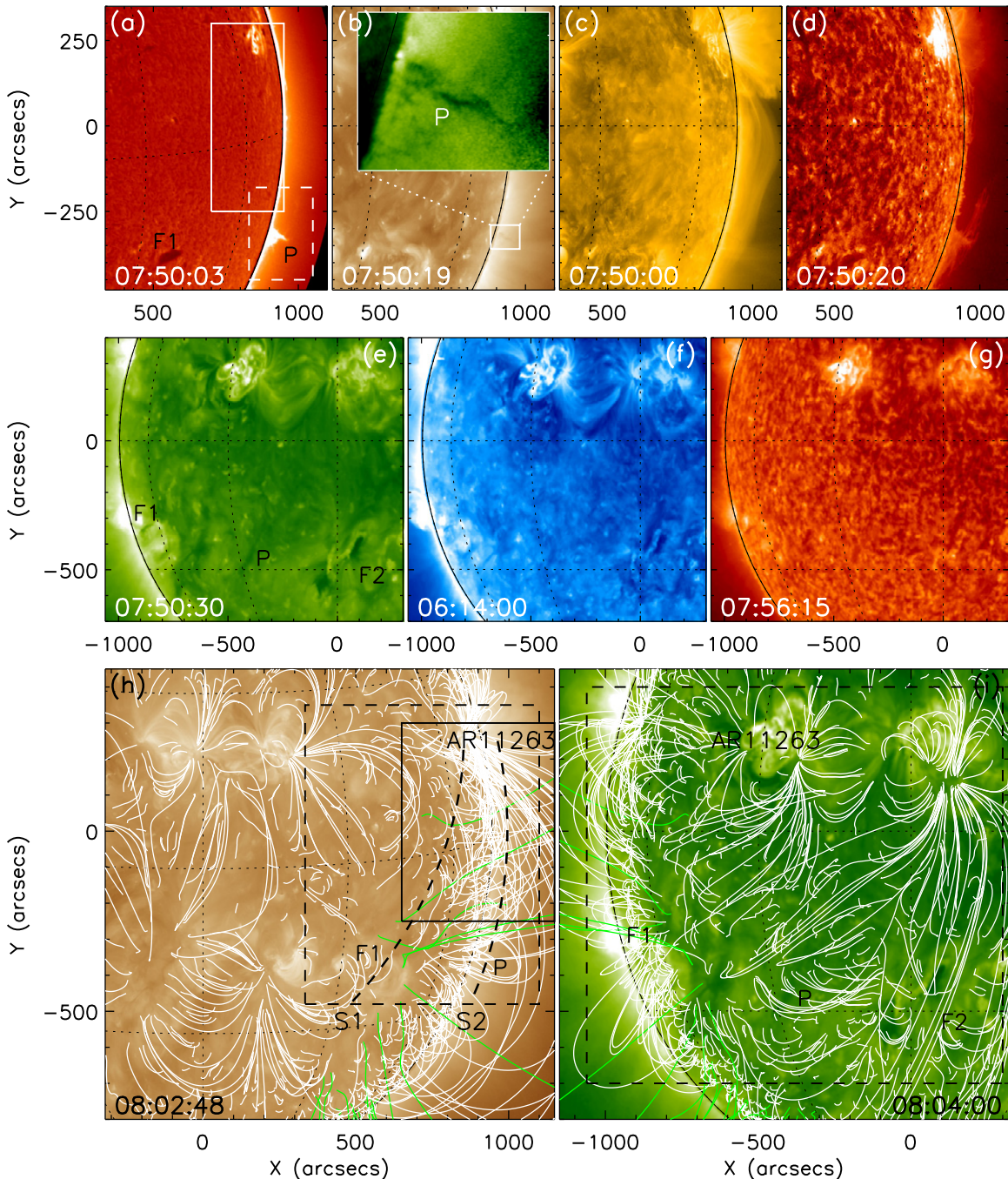


Figure 2. Overview of the event right before the flare. Panel (a) is a SMART $H\alpha$ center image (see also animation 1), and panels (b)–(d) are AIA 193 (animation 2), 171, and 304 \AA images, respectively. The inset in panel (b) is a closed up view of the prominence. Panels (e)–(g) are *STEREO*-Ahead 195 (animation 3), 171, and 304 \AA images, respectively. Panels (h) and (i) are AIA 193 \AA and *STEREO*-Ahead 195 \AA images, respectively. They are overlaid with extrapolated three-dimensional coronal fields, in which the white (green) lines represent the closed (open) field lines. The fields of view of the top and middle rows are indicated by the black dashed boxes in panels (h) and (i), respectively. F1, F2, and P in panels (a) and (e) indicate the two filaments and the prominence, respectively. (A color version of this figure is available in the online journal.)

3.2. The Shock Wave

The shock wave was observed as a fast Moreton wave in the SMART $H\alpha$ observations. However, due to the low cadence of SMART, the Moreton wave can only be observed in three successive images (see animation 1). We show the Moreton wave in the $H\alpha$ center based-difference and Doppler velocity images in Figure 3. To compare Moreton waves in the chromosphere and the corresponding wave signature in the low corona, we also show the AIA 193 \AA based-difference images in the

figure (see animations 2 and 3). It should be pointed out that the based-difference images are created by subtracting a pre-event image from the time sequence images, and the Doppler velocity images are obtained by subtracting the near-simultaneous blue-wing image from the corresponding red-wing one. In the based-difference $H\alpha$ images, the moving wavefront is seen as a white arc-shaped structure, while in the Doppler velocity images the white wavefront (redshift) is followed by a dark one (blueshift), which suggests that the dense chromosphere plasma was first compressed downward (redshift) and then restored

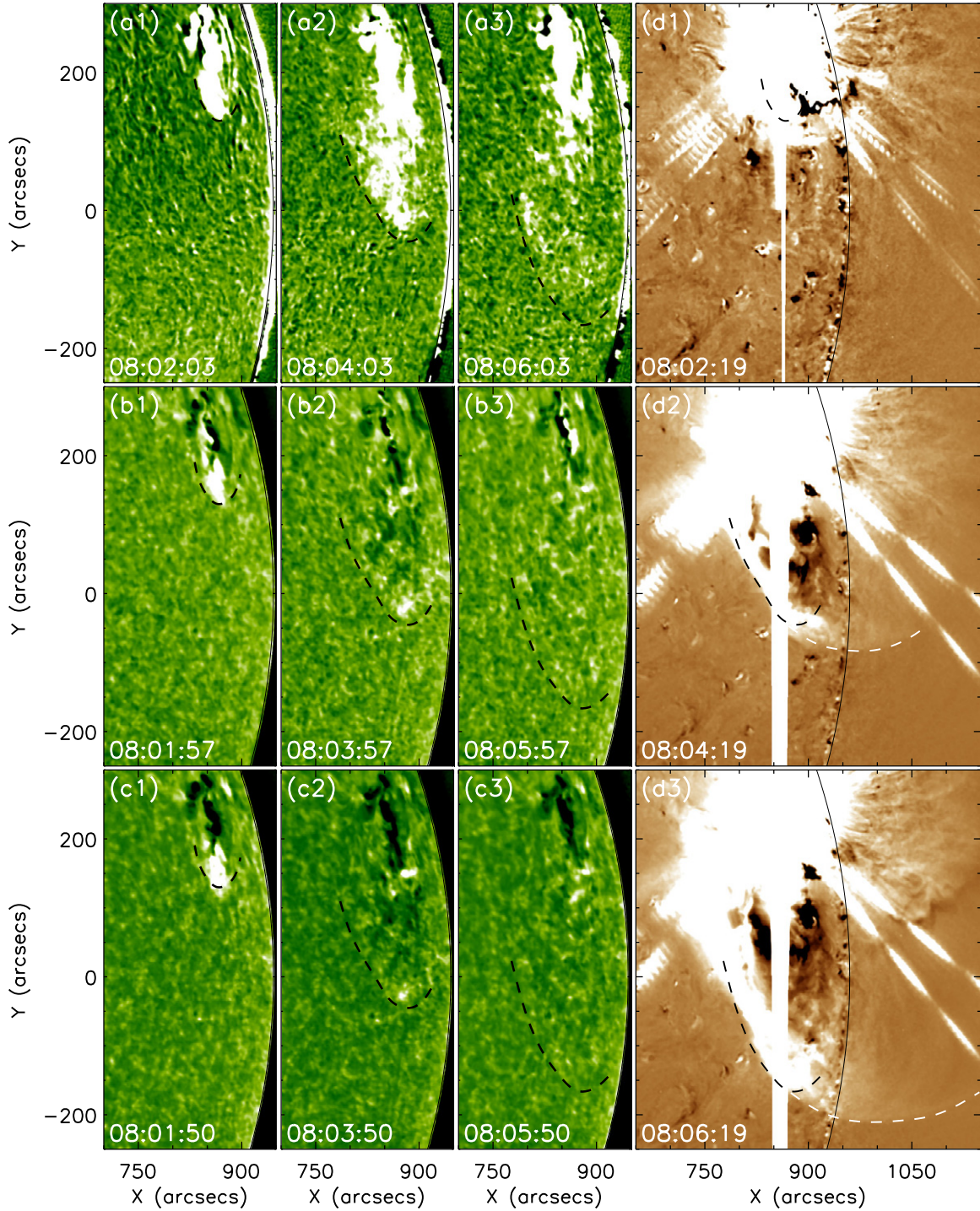


Figure 3. Chromosphere and coronal observations of the shock wave. Panels (a1)–(a3) are SMART $H\alpha$ center based-difference images, while panels (b1)–(b3) and (c1)–(c3) are Doppler velocity images of $H\alpha$ 0.5 and 0.8 \AA from the $H\alpha$ line center. Panels (d1)–(d3) are AIA 193 \AA based-difference images. The black dashed curves indicate the surface of the shock wave, while the white dashed curves indicate the edge of the dome component of the shock wave. The FOV of the $H\alpha$ observations is shown as the white box in Figure 2(a), while that for the AIA 193 \AA is indicated by the black box in Figure 2(h).

(A color version of this figure is available in the online journal.)

upward (blueshift) after the passing of the shock wave. On the other hand, one can see that the coronal wave is composed of two parts in the based-difference AIA 193 \AA images: a sharp arch-shaped bright structure on the disk and a dome-shaped structure over the limb. By comparing the wavefronts in the chromosphere and the low corona, we find that the sharp wave structure in the corona is consistent with the chromosphere Moreton wave due to their similar structure and kinematics (see the dashed

black curves in Figures 3(d1)–(d3)). As one can see from the figure, the dome-shaped structure is smoothly connected to the sharp one. This picture indicates that the coronal shock wave should be in a dome shape, whose lower part sweeps the solar surface and thereby forms the sharp wavefront in the corona and the Moreton wave in the chromosphere (Shen & Liu 2012c; Asai et al. 2012). The EUV and $H\alpha$ observations also suggest that the wave was inclined to the solar surface. These observational

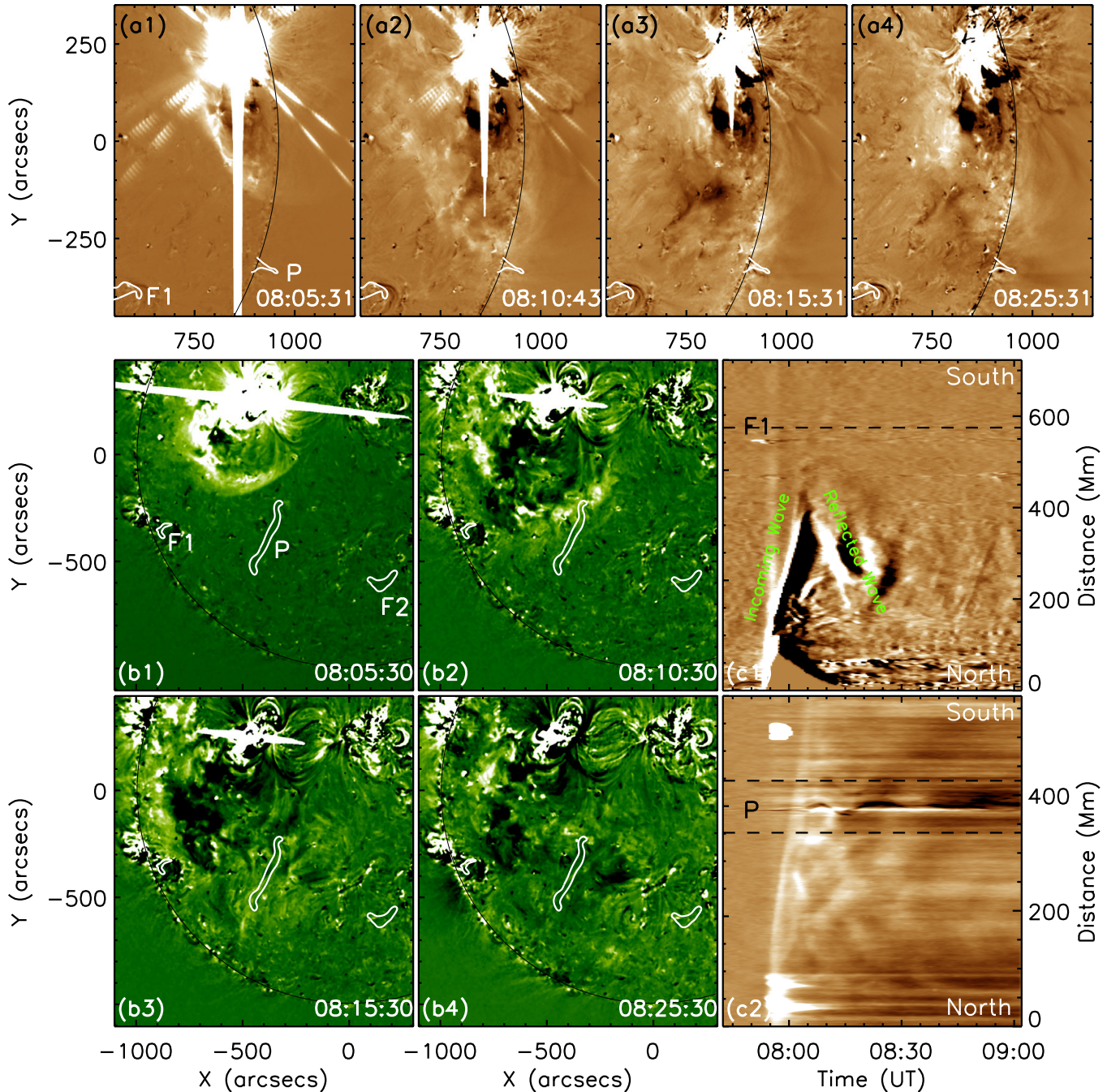


Figure 4. *SDO* and the *STEREO*-Ahead observations of the shock wave (animation 4). Panels (a1)–(a4) and (b1)–(b4) are *SDO*/AIA 193 Å and *STEREO*-Ahead 195 Å based-difference images, respectively. The white contours mark the position of the filaments and the prominence. Panels (c1) and (c2) are time–distance diagrams made from the AIA 193 Å based-difference observations along S1 and S2 as shown in Figure 2(h), respectively. The locations of the filament (F1) and the prominence (P) are indicated by the black horizontal dashed lines in the time–distance diagrams. The fields of view of panels (a1)–(a4) and (b1)–(b4) are shown as black dashed boxes in Figures 2(h) and (i), respectively.

(A color version of this figure is available in the online journal.)

results are in agreement with the theoretical interpretation in Uchida (1968) and recent observations (Liu et al. 2012, 2013), where the chromosphere Moreton wave is caused by the compression of the chromosphere material by a coronal fast-mode shock wave.

Figure 4 shows the shock wave in AIA 193 Å and *STEREO*-Ahead 195 Å observations, in which the locations of the two filaments and the prominence are indicated by the white contours in the figure. We find that the prominence observed in AIA images corresponds to the south leg of the filament in the

STEREO-Ahead observations. It can be identified that the wave first interacted with the filament’s northern leg at about 08:10:30 UT. The wave arrives at F1 and F2 at about 08:15:30 and 08:25:30 UT, respectively. When the wave approaches F1, it encounters strong reflection due to the open fields in its northern side (see Figures 2(h) and (i)). The reflected wave can also be observed in the AIA observations. We show the incoming and reflected waves by means of time–distance diagram technique, in which the propagating shock wave can be identified as a bright stripe. As one can see in the time–distance diagram, the

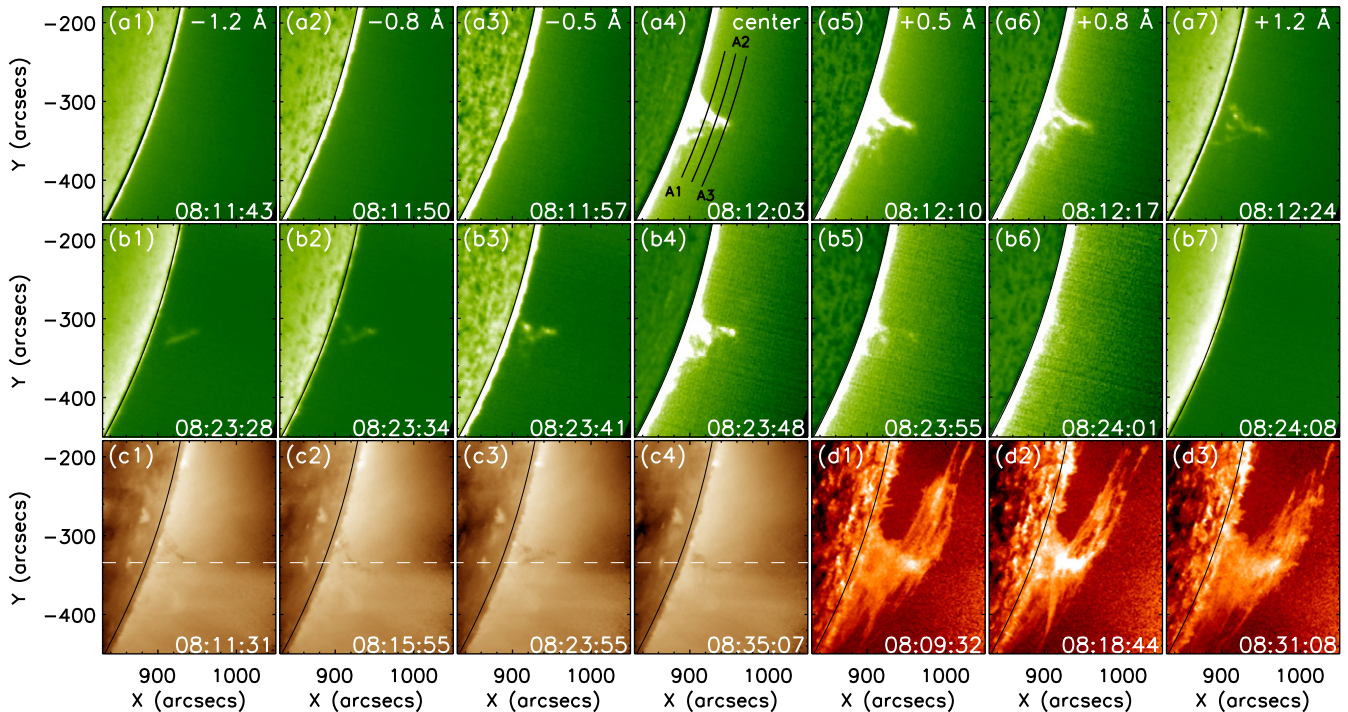


Figure 5. $H\alpha$ and EUV observations of the prominence oscillation. The top and middle rows show the SMART $H\alpha$ line center and line wing at about 08:12 UT and 08:23 UT, respectively. The wavelength for each column of the top two rows is indicated in the top row. Panels (c1)–(c4) are AIA 193 Å images, in which the white dashed line indicates the equilibrium position of the prominence. Panels (d1)–(d3) are AIA 304 Å observations. The field of view of each panel is shown as the white dashed box in Figure 2(a).

(An animation and a color version of this figure are available in the online journal.)

slopes of the incoming and reflected shock waves are positive and negative, respectively (see Figure 4(c1)). One can see that the wave was reflected at a distance of about 450 Mm from the flare site, which is about 150 Mm from F1. This finding could be another possible reason for explaining the weak oscillation of F1, since the reflection of the shock wave can significantly reduce the wave energy. Since the intensity profile of coronal shock waves usually has a Gaussian shape (Wills-Davey 2006), the trajectory of the wavefront can be obtained by fitting the intensity profiles using a Gaussian model (see also Long et al. 2011). In addition, Byrne et al. (2013) found that the Savitzky–Golay filter (Savitzky & Golay 1964) is a more appropriate technique for deriving the kinematics of shock waves than the traditional three-point Lagrangian method. Therefore, in this paper we chose this method to derive the kinematics of the shock wave and the oscillating filament and prominence. The results show that the average speeds of the incoming and the reflected waves are $459.7 \pm 81.3 \text{ km s}^{-1}$ and $-224.8 \pm 67.4 \text{ km s}^{-1}$, respectively. Here, the errors are the standard deviation of the derived velocities. One can see that the speed of the reflected wave is about half of the incoming wave, which indicates the significant energy loss during the interaction process. Panel (c2) shows the wave–prominence interaction process along S2, which reflects the kinematics of the dome-shaped wave component. One can see that the prominence starts to oscillate right after the passing of the shock. The average speed of the shock obtained from this time–distance diagram is $624.6 \pm 134.2 \text{ km s}^{-1}$, which is faster than the on-disk wave component ($459.7 \pm 81.3 \text{ km s}^{-1}$). The discrepancy of the speed of the two components is possibly the result of wave delay at lower heights in the solar atmosphere due to the forward inclining structure of the shock wave (Liu et al. 2012, 2013), or larger magnetic field strength at lower altitude.

3.3. The Transverse Oscillation of the Prominence

Figures 5–7 show the detailed analysis results of the transverse oscillating prominence. First of all, we display the $H\alpha$ Doppler and multi-wavelength EUV observations in Figure 5 to show the intriguing prominence oscillation and the wave–prominence interaction processes (see animation 4). In the $H\alpha$ observations, the prominence is located at the west limb, and it can only be observed in the $H\alpha$ center images before the oscillation. Immediately after the passing of the shock wave, the prominence appeared in the $H\alpha$ red-wing observations, which indicates that the prominence was pushed to westward by the shock wave (see the top row in Figure 5). Several minutes later, the prominence appeared in the blue-wing images and disappeared from the red-wing observations (see the middle row in Figure 5). This indicates that the prominence changed the westward motion (redshift) to eastward (blueshift) during this period. The motion pattern of the prominence is similar to the on-disk observations of winking filaments induced by shock waves (e.g., Shen et al. 2014). The observational results also indicate that the axis of the prominence is not strictly along the north–south direction, as in that case, no Doppler motion could be detected in the $H\alpha$ -wing observations. The oscillating prominence is also shown in AIA 193 Å and 304 Å images (see the bottom row in Figure 5). We find that in 193 Å images the prominence first moved to the south and then to the north. Taking the Doppler $H\alpha$ and the AIA imaging observations together into consideration, such a kinematics pattern suggests that the resultant motion of the prominence should be first in the southwest and then in northeast direction, and the axis of the prominence is along northeast–southwest direction as shown by the *STEREO*-Ahead on-disk observations (see Figures 4(b1)–(b4)). In the AIA 304 Å images, the interaction of the wave and the prominence can be

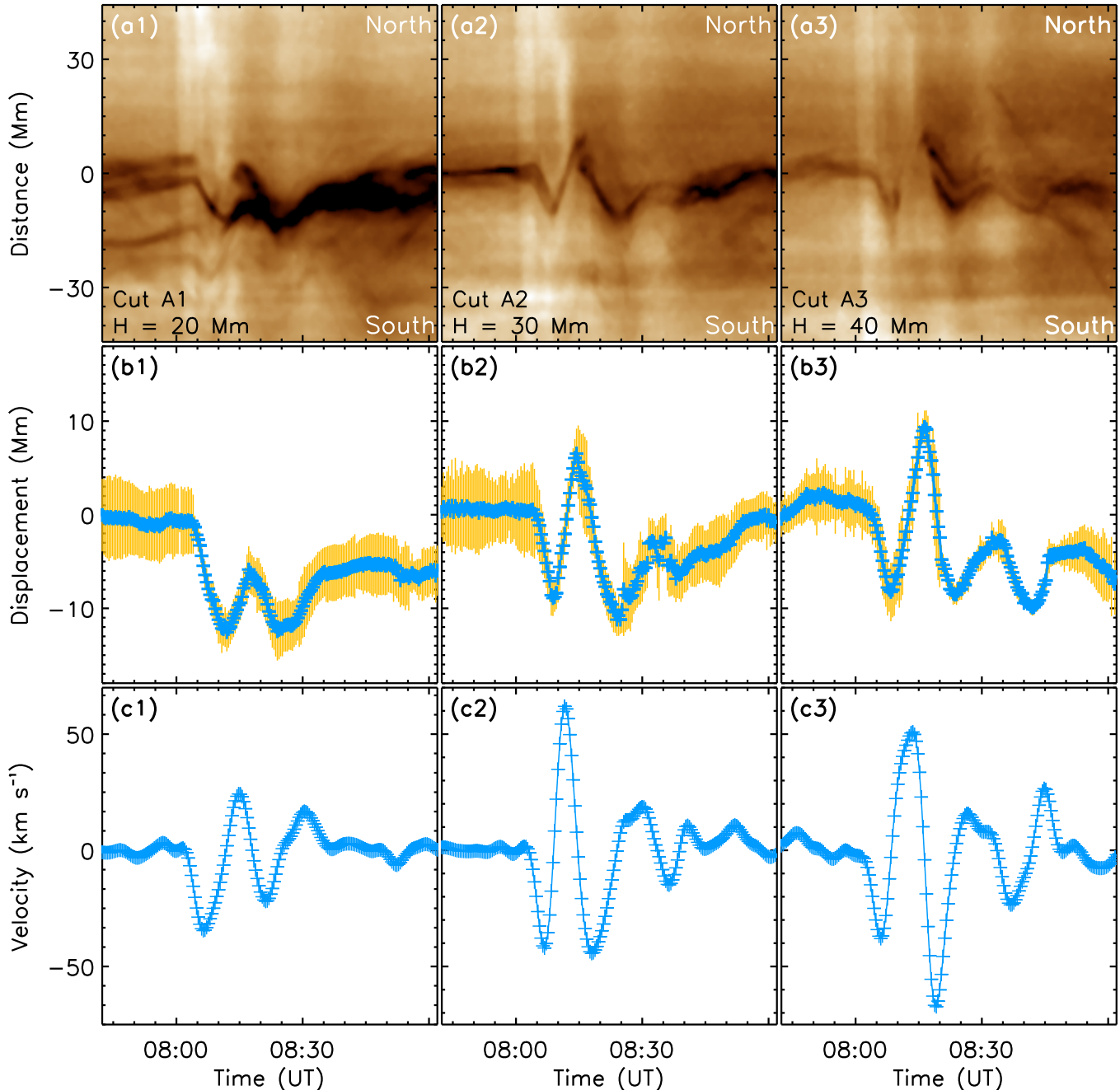


Figure 6. AIA 193 Å analysis of the oscillating prominence. The top row shows the time–distance diagrams obtained from 193 Å images along cuts A1–A3 (see Figure 5(a4)), whose heights are 20, 30, and 40 Mm from the solar limb, respectively. The middle and bottom rows show the corresponding trajectory and velocity, respectively. The golden vertical bars show the measuring errors of the prominence trajectory, which are given by the widths of the Gaussian fit applied to the intensity profiles. In each frame, the solar north (south) is up (down), while the equilibrium position of the prominence is set as the original point of the prominence oscillation. (A color version of this figure is available in the online journal.)

identified by tracing the brightening caused by the compression of the wave to the prominence material (see panels (d1)–(d3) in Figure 5 and animation 4), which is possibly useful for diagnosing the properties of the prominence magnetic fields and the wave energy loss of the shock wave during the interaction.

We measure the transverse motion of the oscillating prominence at three different heights, i.e., 20, 30, and 40 Mm above the solar limb as indicated by the three curves in Figure 5(a4). Along these cuts, we first generate the time–distance diagrams using the time sequence AIA 193 Å and H α center images, and then we are able to trace the trajectory of the oscillating prominence and derive the oscillation velocity profile. The time–distance

diagrams obtained from the AIA 193 Å images are shown in the top row of Figure 6. The position of the prominence at a certain time is determined by fitting the intensity profile using a Gaussian profile, and the error is given by the width of the Gaussian. The traced trajectory (blue) and the associated error (golden) of the oscillating prominence is plotted in the middle row, from which we also derived the velocity profile at the three heights using the Savitzky–Golay filter method (bottom row). This figure clearly shows that the prominence starts to oscillate immediately after the arrival of the shock wave, and the oscillation lasts for about two cycles. In addition, the oscillation amplitude at higher altitudes is larger than that at lower heights,

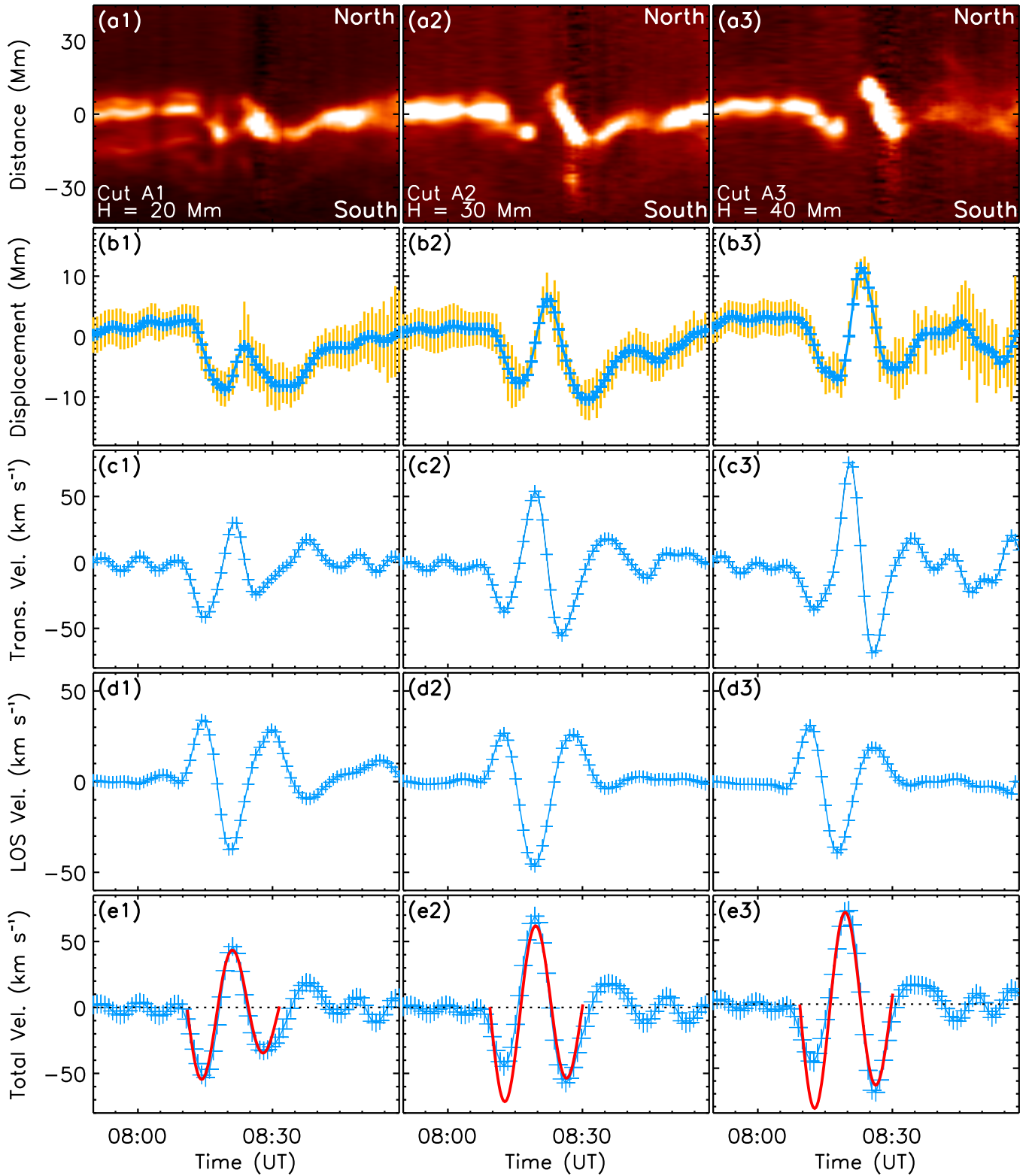


Figure 7. SMART analysis of the oscillating prominence. The top row shows the time–distance diagrams obtained from $H\alpha$ center images along cuts A1–A3 (see Figure 5(a4)), whose heights are 20, 30, and 40 Mm from the solar limb, respectively. The second row shows the corresponding trajectories (blue) with error bars (golden) given by the widths of the Gaussian fit applied to the intensity profiles along the cuts. The third, fourth, and bottom rows show the derived transverse, LOS, and the resultant three-dimensional velocities, respectively. The red curves in the bottom row are the fitting result to the total velocity profiles. In each panel, north is up and south is down.

(A color version of this figure is available in the online journal.)

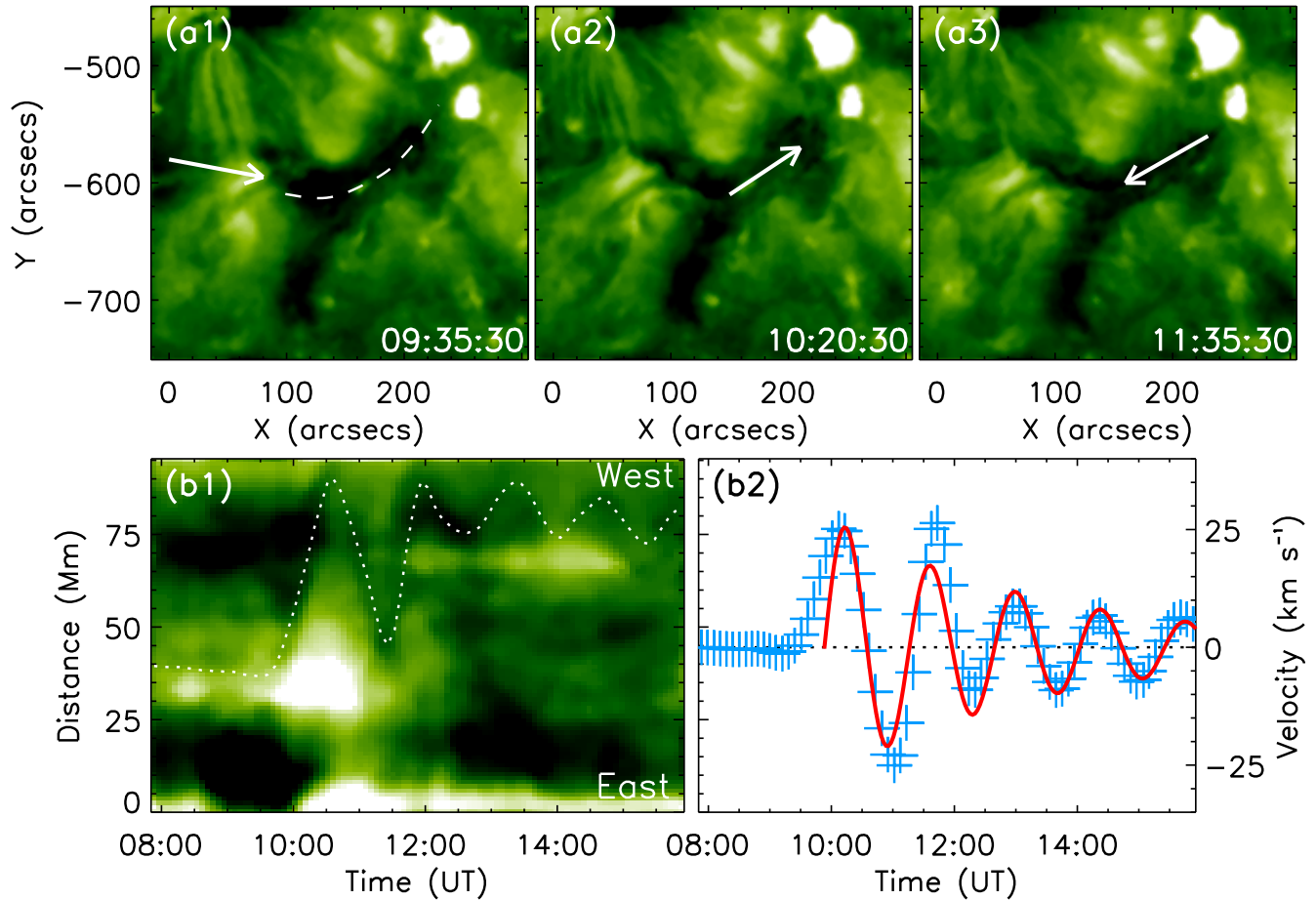


Figure 8. *STEREO*-Ahead observations of the longitudinal oscillation in F2 (see also animation 3). Panels (a1)–(a3) are 195 Å images, in which the white arrow in panel (a1) indicates the propagating direction of the incoming wave, while those in panels (a2) and (a3) indicate the moving direction of the oscillating filament mass. Panel (b1) is a time–distance diagram obtained from 195 Å images along the filament axis as shown by the white dashed curve in panel (a1). The traced trajectory of the oscillating mass is overlaid on the time–distance diagram as a white dotted curve. Panel (b2) shows the derived oscillation velocity (blue) and the fitting result (red) of the velocity profile.

(An animation and a color version of this figure are available in the online journal.)

which suggests that the prominence oscillates like a vertical linear rigid body with its one end anchored on the solar surface.

Figure 7 shows the analysis results obtained from H α observations. The time–distance diagrams are shown in the top row, based on which we further derived the trajectories (second row) and transverse velocities (third row) at different heights with the same method used in Figure 6. In addition, using the Doppler observations taken using the SMART telescope and Beckers’ cloud model (Beckers 1964), we also derive the Doppler velocity along the line of sight (LOS). The cloud model is a widely used method for deriving parameters of cloud-like structures in the solar corona (e.g., Liu & Ding 2001a, 2001b; Morimoto & Kurokawa 2003; Morimoto et al. 2010; Shen et al. 2014). To obtain the Doppler velocity of the oscillating prominence, one first needs to measure the intensity contrast profile of a point on the prominence. Here, the intensity contrast is obtained by dividing the prominence intensity by the nearby background intensity. Then, fitting the intensity contrast profile with the cloud model, one can obtain the four unknown parameters in the cloud model, namely, the source function S , the Doppler width $\Delta\lambda_D$, the optical thickness τ_0 , and the Doppler velocity v . Since a detailed description of the cloud model can be found in many articles (e.g., Tziotziou 2007; Shen et al. 2014 and references therein), we do not describe it in this paper. The derived Doppler velocities at different heights are shown in the fourth row of Figure 7.

It is clear that the phase difference between the Doppler velocity and the transverse velocity is about π , which suggests that the southward (northward) motion of the prominence in imaging observations corresponds to the redshift (blueshift) motion in the Doppler images. This result indicates that the orientation of the prominence axis should be in northeast–southwest direction, in agreement with the on-disk observational results based on the *STEREO*-Ahead images. Finally, the total three-dimensional velocity can be obtained by compositing the transverse and the Doppler velocity components obtained from the H α observations. The results are shown in the bottom row of Figure 7. To obtain the oscillation periods of the oscillating prominence at different heights, the total velocity profiles are fitted with a damping function in a form of $F(t) = A \exp(-t/\tau) \sin((2\pi t/T) + \phi)$, where A , T , τ , and ϕ are the initial amplitude, period, damping time, and initial phase, respectively (see the overlaid red curves). The same fitting procedure is also applied to the transverse oscillation velocity profiles obtained from AIA 193 Å (the bottom row of Figure 6) and H α center (the third row of Figure 7) observations, and the results are all listed in table 1. One can see that the prominence oscillation has a larger velocity amplitude at the higher altitude, but the oscillation periods at different heights are the same (13.5 minutes). In addition, the damping time at higher height is also larger than that at lower height, which may indicate the

Table 1
Various Parameters of the Oscillating Prominence

Height (Mm)	$A_{\text{Tran}193}$ (km s^{-1})	$A_{\text{Tran}H\alpha}$ (km s^{-1})	A_{LOS} (km s^{-1})	A_{Tot} (km s^{-1})	P_{Tot} (minute)	τ_{Tot} (minute)
20	33.4 ± 2.4	37.8 ± 4.5	33.8 ± 2.5	65.3 ± 3.3	13.5 ± 0.1	31.3 ± 4.2
30	52.7 ± 5.3	55.6 ± 3.9	38.2 ± 4.6	78.1 ± 2.6	13.5 ± 0.2	45.3 ± 2.7
40	84.3 ± 4.8	82.7 ± 4.2	40.7 ± 3.1	89.6 ± 4.1	13.5 ± 0.1	54.0 ± 4.1

Notes. “Height” is the three measured heights as shown in Figure 4(a4). $A_{\text{Tran}193}$ and $A_{\text{Tran}H\alpha}$ are the transverse velocity amplitude measured from AIA 193 Å and H α observations, while A_{LOS} and A_{Tot} are the Doppler velocity amplitude in the LOS and the derived total velocity amplitude, respectively. P_{Tot} and τ_{Tot} are the period and damping time obtained from the total velocity profile, respectively. The errors are the standard deviation yields using the fitting procedure.

different magnetic field and plasma density of the surrounding corona at these heights.

3.4. The Longitudinal Oscillation in F2

From the view angle of *STEREO*-Ahead, it is interesting that large-amplitude longitudinal oscillation is observed in the other filament (F2) after the passing of the shock wave. In previous articles, the initiation of such filament oscillation is often due to the nearby micro flares, jets, and filament eruptions. However, in this case, it is evidenced that the longitudinal oscillation in F2 is directly caused by the shock wave. This is the first report of large-amplitude filament oscillations initiated by the shock wave. Since there were no H α and *SDO* observations of this filament, we can only show the *STEREO*-Ahead observations in Figure 8. As one can see in panels (a1)–(a3) of Figure 8 and animation 3, F2 is oriented in the east–west direction. The shock wave came from the east and first interacted with the eastern end of the filament. Then, part of the filament mass started to oscillate along the main axis of the filament. The incoming wave is indicated by the white arrow in Figure 8(a1), and the direction of the mass motion is indicated by the white arrows in Figures 8(a2) and (a3). To study the kinematics of the oscillation, we further generate the time–distance diagram along the filament axis (dashed curve in Figure 8(a1)), and the result is plotted in Figure 8(b1). Since the cut is along the filament axis that is full of dark filament mass, it is difficult to trace the oscillating trajectory due to the low signal-to-noise ratio. Therefore, we simply trace the oscillation trajectory by eye from the time–distance diagram (white dotted curve in Figure 8(b1)). Using the Savitzky–Golay filter method, the velocity profile (blue) is derived from the traced trajectory (blue curve in Figure 8(b2)). The velocity profile is then fitted with the damping function $F(t) = A \exp(-t/\tau) \sin((2\pi t/T) + \phi)$ (red curve in Figure 8(b2)). The results show that the filament oscillated about four cycles, and the period and velocity amplitude are about 80.3 ± 3.6 minutes and $26.8 \pm 3.1 \text{ km s}^{-1}$. It can be seen that the first cycle shows a large amplitude, and then it quickly decreases to a moderate value. This characteristic is consistent with the idea that the oscillation is launched by the arriving of the shock wave, which can exert a pulse-like pressure to the filament mass in the axial direction and thus drives the longitudinal motion in the filament.

4. CONCLUSIONS AND DISCUSSIONS

The impulsive X6.9 flare on 2011 August 9 is so far the strongest flare during the current solar cycle, and it has attracted

a lot of attention from solar physicists. Several authors have studied the different aspects of this flare (Shen & Liu 2012c; Asai et al. 2012; Tan & Tan 2012; Srivastava & Goossens 2013; Sripathi et al. 2013). However, a detailed study of the filament and prominence oscillations resulting from the shock wave has not been performed. In this paper, we present the first observations of simultaneous transverse oscillations of a prominence (P) and a filament (F1) and the longitudinal oscillation of another filament (F2) launched by the large-scale shock wave in association with the impulsive flare, using the high temporal and spatial resolution Doppler and stereoscopic observations taken using the ground-based SMART and spaceborne *SDO* and *STEREO* instruments. In addition, we also derive the three-dimensional velocity and other parameters of the oscillating prominence, which are important for further theoretical and numerical investigations of the prominence nature.

In EUV observations, it is evident that the shock wave is composed of two distinct components: one is the sharp arc-shaped wavefront propagating on the surface ($v_{av} = 459.7 \text{ km s}^{-1}$), and the other is the dome-shaped wave structure over the limb ($v_{av} = 624.6 \text{ km s}^{-1}$). The former has topology and kinematics similar to the wave signatures observed in AIA 1700 Å, 1600 Å, and H α observations, which image the transition region and chromosphere layers below the corona (Shen & Liu 2012c). When the sharp surface component of the shock wave encountered a region of open magnetic fields, it underwent a reflection process that reduced the wave speed to about 224.8 km s^{-1} . The speed of the reflected wave is about half of the incoming wave, which indicates significant energy loss of the shock wave during the interaction with the open fields. The smooth connection of the two wave components suggests that the sharp wave structure on the surface should be caused by the compression of the surface plasma by the dome-shaped shock wave, in agreement with the theoretical prediction in Uchida (1968). The shock wave resulted in the oscillation of a prominence (P) over the limb and two filaments (F1 and F2) on the disk. Using a pair of *SDO* 193 Å and *STEREO*-A 195 Å images before the flare, the three-dimensional structures of F1 and the prominence are reconstructed, and their heights above the solar surface are about 34.8 and 79.0 Mm, respectively. We find that F1 showed weak oscillation after the passing of the shock wave (not shown here), unlike the strong oscillation of the prominence and F2. Based on our analysis results, we propose that the weak oscillation of F1 is possibly due to two reasons: the lower altitude of the filament and the weakening of the shock wave due to the reflection by the nearby open magnetic fields.

The prominence showed obvious transverse oscillation after the passing of the shock wave. Using the H α Doppler observations taken by the SMART and Beckers’ cloud model, we first derive the three-dimensional velocity of the oscillating prominence, based on the measurement of the transverse velocity in the plane of sky and the Doppler velocity along the LOS direction. The oscillation parameters at the three heights (20, 30, and 40 Mm above the surface) on the prominence are measured. The results indicate that at higher heights, the oscillation amplitude is larger than those at lower altitudes, but the oscillation periods at different heights are all the same (13.5 minutes). This suggests that the prominence oscillates like a linear vertical rigid body with its one end anchored to the Sun. In addition, the damping time at a higher height is also larger than that at a lower height, which suggests that at lower heights the damping is more serious than that at higher heights. This result reflects the different

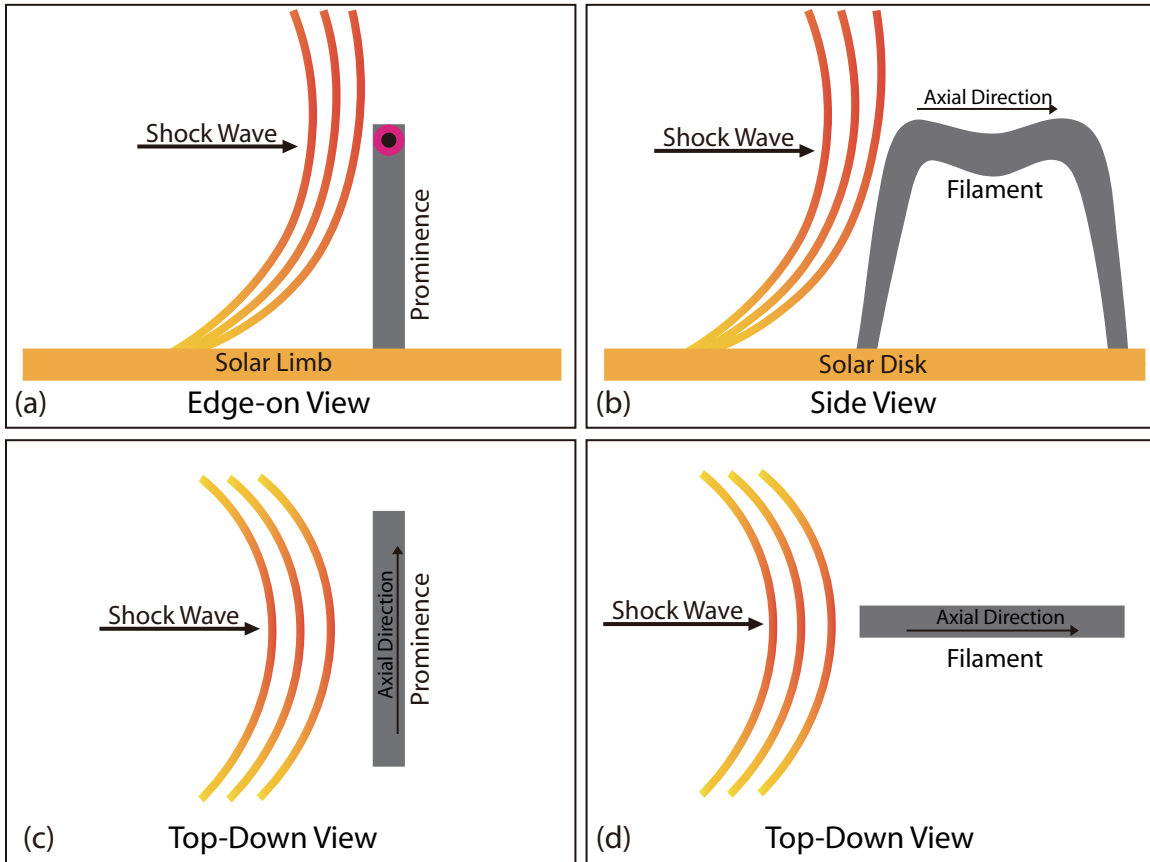


Figure 9. Cartoon demonstration of the wave–prominence and wave–filament interaction processes. Panels (a) and (b) are the edge-on and side views of the prominence and the filament, while panels (c) and (d) are the top-down views of panels (a) and (b), respectively. The propagation direction of the shock wave is indicated by the black arrow on the left, and red curves represent the propagating wavefront right before the interactions. The axis of the prominence is indicated by a red circle on the top of the prominence in panel (a), while the filament axis is indicated by the thin black arrow in panel (b). The axial directions of the prominence and the filament are also indicated by the black thin arrows in panels (c) and (d), respectively.

(A color version of this figure is available in the online journal.)

magnetic field strengths and plasma densities of the surrounding corona at these heights. Based on the fitting results of the derived three-dimensional velocity profiles, at the heights of 20, 30, and 40 Mm above the surface, the oscillation velocity amplitudes are about 65.3, 78.1, and 89.6 km s^{-1} ; the periods are all 13.5 minutes; and the damping times are about 31.3, 45.3, and 54.0 minutes, respectively. F2 can only be observed from the *STEREO*-Ahead angle of view; therefore, we cannot measure the three-dimensional parameters of this filament. However, after the passing of the shock wave, an intriguing large-amplitude longitudinal oscillation is observed in this filament, which is the first observation of longitudinal oscillation in filaments induced by a large-scale coronal shock wave. The longitudinal oscillation lasts for about four cycles, and it shows a large amplitude during the first cycle and then quickly decreases to a moderate value due to some unknown damping mechanisms. Our analysis results indicate that the initial velocity amplitude and oscillation period of the longitudinal oscillation are about 26.8 km s^{-1} and 80.3 minutes, respectively. We propose that the longitudinal oscillation in F2 is directly launched by the interaction of the shock wave, which can exert a pulse-like pressure on the filament mass in the axial direction and thus drives the longitudinal oscillation along the filament axis.

The stereoscopic and Doppler observations of filament oscillations are useful for diagnosing the magnetic structure and properties of filaments and shock waves, and the derived

three-dimensional information on the prominence oscillation can provide important initial input parameters to further the numerical and theoretical investigations of the prominence nature, because the three-dimensional results have removed the measuring errors resulting from projection effects when one uses two-dimensional imaging observations. As one can see in Figure 3, the shock wave has a dome-shaped structure, and evidently the wavefront is inclined to the solar surface. Such a configuration of coronal shock waves has also been proposed theoretically (Uchida 1968) and confirmed in a few recent observational studies (e.g., Liu et al. 2012, 2013). Since the speed of a fast MHD wave is faster in the corona than that in the dense chromosphere, the propagation of a shock wave in the chromosphere should delay to its coronal counterpart. However, due to the low cadence of the *SMART* observation, it is difficult to identify such a phenomenon in this event. On the other hand, it is well-known that prominences or filaments are coronal structures that are cool plasmas supported by coronal magnetic fields (e.g., Kippenhahn & Schlüter 1957; Kuperus & Raadu 1974). Therefore, the height of the interaction positions between the shock wave and the prominence and filaments should be high in the low corona. The interaction between the shock wave and the prominence presented in this paper should be a good example for demonstrating such a process. Similar to the scenario presented in Vršnak et al. (2002) and Warmuth et al. (2004), we draw a cartoon in Figure 9 to illustrate the interaction processes

between the shock wave and the prominence and the filament. We consider the prominence to be a linear vertical magnetic structure with the roots of one end on the Sun. When the shock wave arrives, the interaction between the wave and the prominence should take place at the top end of the prominence, and the normal vector of the shock is perpendicular to the prominence axis. The edge-on and top-down views of the wave–prominence interaction process are shown in panels (a) and (c), respectively. Due to the inclined topology of the shock wave, the pressure impact on the prominence should point to the bottom-right direction. Therefore, the initial displacement of the prominence is naturally in this direction. After the passing of the shock wave, the prominence will oscillate freely in the corona for a few cycles. The interaction of the shock wave and F2 is shown in Figures 9(b) (side view) and (d) (top-down view). Here, the axis of the filament is parallel to the normal vector of the shock wave during the interaction period. Therefore, the arrival of the shock wave will press the filament mass to move longitudinally along the filament axis. After the passing of the shock wave, the filament mass will oscillate freely in the filament channel. It should be noted that the driving mechanism of longitudinal oscillations in filament launched by a shock wave is different from those by activities of micro jets, flares, and filament eruptions, which can inject poloidal magnetic flux into the filament tube through magnetic reconnection at one of the filament legs and thereby launches the longitudinal filament oscillation (Vršnak et al. 2007). We would like to emphasize that a shock wave can launch not only transverse but also longitudinal filament oscillations, and the orientation of the filament relative to the wave vector should be important for launching transverse or longitudinal filament oscillations. Namely, when the normal vector of the shock wave is parallel to the filament axis, longitudinal oscillation in the filament can be expected; otherwise, one can expect transverse oscillation of the filament.

It is well known that filaments or prominences are cool plasma supported by a coronal magnetic field, and there are two classical models that have been widely accepted by solar physicists, i.e., the Kippenhahn–Schlüter (Kippenhahn & Schlüter 1957) and Kuperus–Raadu (Kuperus & Raadu 1974) models. The cool and dense filament mass resides in a magnetic dip and can remain stable due to the balance between the downward gravity and upward magnetic force. In this line of thought, the restoring force for transverse filament oscillations should be the coupling of gravity and magnetic tension. As for large-amplitude longitudinal oscillations in filaments, the moving magnetized filament plasma along the filament tube would change the distribution of the filament magnetic field (especially in the case of a helical supporting magnetic field structure), which can produce a pressure gradient force opposite to the moving direction of the filament mass. As proposed by Vršnak et al. (2007), the magnetic pressure gradient along the filament axis can probably be the restoring force. However, if we consider that the filament mass oscillates in a curved magnetic dip, one cannot ignore the gravity and magnetic tension contribution to the restoring force. Therefore, the restoring force of longitudinal filament oscillation is probably the resultant force of gravity and magnetic pressure.

Using the derived parameters of the oscillating prominence and filaments, we can estimate the strength of the supporting magnetic fields. For the transverse oscillating prominence, the radial component of the prominence magnetic field can be estimated using the method proposed by Hyder (1966). The relation between the radial magnetic field and the

oscillation period and damping time can be written as $B_r^2 = \pi \rho r_0^2 [4\pi^2 (1/T)^2 + (1/\tau)^2]$, where B_r is the radial magnetic component, ρ is the density of the prominence mass, r_0 is the scale height of the prominence, T is the oscillation period, and τ is the damping time. If we use the value $\rho = 4 \times 10^{-14} \text{ g cm}^{-3}$, i.e., $n_e = 2 \times 10^{10} \text{ cm}^{-3}$, the above equation can be rewritten in the form $B_r^2 = 4.8 \times 10^{-12} r_0^2 [(1/T)^2 + 0.025 (1/\tau)^2]$. With the measured oscillation periods and damping times, we obtain a value of the radial component of the prominence’s magnetic fields B_r at heights of 20, 30, and 40 Mm above the solar limb of 8.13, 8.12, and 8.12 gauss, respectively. In the calculation, we use the value $r_0 = 3 \times 10^9 \text{ cm}$ (Hyder 1966). The results appear to show that the prominence has the same radial magnetic field strength at different heights along its main axis. However, one should keep in mind that the plasma densities at different heights are set to the same value in our calculation. For the longitudinal oscillating filament, one can derive the poloidal field in the equilibrium state with the simple equation given by Vršnak et al. (2007), where the authors found that $P \approx 4.4L/v_{A\phi}$. In the formula, P is the filament oscillation period, L is half the filament length, $v_{A\phi} = (B_{\phi 0})/(\sqrt{\mu_0 \rho})$ represents the Alfvén speed based on the equilibrium poloidal field $B_{\phi 0}$. The measured L is about 54.78 Mm. With the derived oscillation period, we obtain that the Alfvén speed $v_{A\phi} \approx 45.48 \text{ km s}^{-1}$. Using the same number density in the above calculation, we obtain that the poloidal field of the filament is about 3.22 gauss.

It has been noted that filaments do not always oscillate when they locate on the path of a shock wave (e.g., Okamoto et al. 2004; Shen et al. 2014). The observation of the weak oscillation of F1 in this case may give some hints to explain such a phenomenon. High-resolution observations have revealed that shock waves always dissipate their energy to thermal or other forms of energy in the ambient medium in which the wave propagates (Thompson & Myers 2009; Shen & Liu 2012b, 2012c; Shen et al. 2013a; Liu & Ofman 2014). For a filament located far from the wave’s source region, the wave energy may decrease too much to launch the oscillation of the filament. In addition, as pointed out in this paper, the low altitude of the filament and the reflection of the shock wave by the nearby magnetic structures are also important for interpreting the weak or non-oscillation filament on the wave path, since the reflection of the shock wave can significantly decrease its energy before the interaction.

In summary, the observations of large-amplitude filament oscillations are important in diagnosing the properties of filaments and shock waves, as well as for predicting a filament eruption. The restoring force and damping mechanisms of large-amplitude transverse and longitudinal filament oscillations are all open questions. In particular, we present the first observations of longitudinal oscillation in a filament induced by a large-scale shock wave. Although a possible driving mechanism is proposed in this paper, it still needs further theoretical and observational investigations in the future.

SDO is a mission of NASA’s Living With a Star (LWS) Program. We thank the SMART and *STEREO* teams for data support. The authors also thank an anonymous referee for constructive suggestions and comments, which greatly improved the quality of this paper. Y.S. is supported by the research fellowship of Kyoto University, and he thanks the staff and students at Kwasan and Hida Observatories for their support and helpful comments on this paper. Y.S. also thanks Dr. W. Liu for

his review of our paper and helpful suggestions on the cartoon demonstration. P.F.C. is supported by the Chinese Foundations NSFC11025314 and 2011CB811402. This work is supported by the Natural Science Foundation of China (11403097), the Specialized Research Fund for State Key Laboratories, the Open Research Program of the Key Laboratory of Solar Activity of Chinese Academy of Sciences (KLSA201401), the Key Laboratory of Modern Astronomy and Astrophysics of Nanjing University, and the Western Light Youth Project of Chinese Academy of Sciences.

REFERENCES

- Arregui, I., Oliver, R., & Ballester, J. L. 2012, *LRSP*, **9**, 2
 Asai, A., Ishii, T. T., Isobe, H., et al. 2012, *ApJL*, **745**, L18
 Beckers, J. M. 1964, PhD thesis, Univ. Utrecht
 Bi, Y., Jiang, Y., Li, H., Hong, J., & Zheng, R. 2012, *ApJ*, **758**, 42
 Bi, Y., Jiang, Y., Yang, J., et al. 2013, *ApJ*, **773**, 162
 Bi, Y., Jiang, Y., Yang, J., et al. 2014, *ApJ*, **790**, 100
 Bruzek, A. 1951, *ZA*, **28**, 277
 Byrne, J. P., Long, D. M., Gallagher, P. T., et al. 2013, *A&A*, **557**, A96
 Chen, P. F. 2011, *LRSP*, **8**, 1
 Chen, P. F., Innes, D. E., & Solanki, S. K. 2008, *A&A*, **484**, 487
 Dodson, H. W. 1949, *ApJ*, **110**, 382
 Dyson, F. 1930, *MNRAS*, **91**, 239
 Eto, S., Isobe, H., Narukage, N., et al. 2002, *PASJ*, **54**, 481
 Fang, C. 2012, *RAA*, **11**, 1377
 Foullon, C., Verwichte, E., & Nakariakov, V. M. 2004, *A&A*, **427**, L5
 Foullon, C., Verwichte, E., & Nakariakov, V. M. 2009, *ApJ*, **700**, 1658
 Gilbert, H. R., Daou, A. G., Young, D., Tripathi, D., & Alexander, D. 2008, *ApJ*, **685**, 629
 Gosain, S., & Foullon, C. 2012, *ApJ*, **761**, 103
 Hershaw, J., Foullon, C., Nakariakov, V. M., & Verwichte, E. 2011, *A&A*, **531**, A53
 Hyder, C. L. 1966, *ZA*, **63**, 78
 Isobe, H., & Tripathi, D. 2006, *A&A*, **449**, L17
 Isobe, H., Tripathi, D., Asai, A., & Jain, R. 2007, *SoPh*, **246**, 89
 Jackiewicz, J., & Balasubramaniam, K. S. 2013, *ApJ*, **765**, 15
 Jing, J., Lee, J., Spirock, T. J., & Wang, H. 2006, *SoPh*, **236**, 97
 Jing, J., Lee, J., Spirock, T. J., et al. 2003, *ApJL*, **584**, L103
 Kaiser, M. L., Kucera, T. A., Davila, J. M., et al. 2008, *SSRv*, **136**, 5
 Kippenhahn, R., & Schlüter, A. 1957, *ZA*, **43**, 36
 Kleczek, J., & Kuperus, M. 1969, *SoPh*, **6**, 72
 Kumar, P., Cho, K.-S., Chen, P. F., Bong, S.-C., & Park, S.-H. 2013, *SoPh*, **282**, 523
 Kuperus, M., & Raadu, M. A. 1974, *A&A*, **31**, 189
 Lemen, J. R., Title, A. M., Akin, D. J., et al. 2012, *SoPh*, **275**, 17
 Li, T., & Zhang, J. 2012, *ApJL*, **760**, L10
 Lin, R. P., Dennis, B. R., Hurford, G. J., et al. 2002, *SoPh*, **210**, 3
 Liu, R., Liu, C., Xu, Y., et al. 2013, *ApJ*, **773**, 166
 Liu, W., Nitta, N. V., Schrijver, C. J., Title, A. M., & Tarbell, T. D. 2010, *ApJ*, **723**, L53
 Liu, W., Ofman, L., Nitta, N. V., et al. 2012, *ApJ*, **753**, 52
 Liu, W., Title, A. M., Zhao, J. W., et al. 2011, *ApJL*, **736**, L13
 Liu, W., & Ofman, L. 2014, *SoPh*, **289**, 3233
 Liu, Y., & Ding, M. D. 2001a, *SoPh*, **200**, 127
 Liu, Y., & Ding, M. D. 2001b, *ChJAA*, **1**, 460
 Liu, Y. D., Luhmann, J. G., Kajdič, P., et al. 2014, *NatCo*, **5**, 3481
 Long, D. M., Gallagher, P. T., McAteer, R. T. J., & Bloomfield, D. S. 2011, *A&A*, **531**, A42
 Luna, M., Díaz, A. J., & Karpen, J. 2012, *ApJ*, **757**, 98
 Luna, M., & Karpen, J. 2012, *ApJL*, **750**, L1
 Luna, M., Knizhnik, K., Muglach, K., et al. 2014, *ApJ*, **785**, 79
 Moreton, G. E., & Ramsey, H. E. 1960, *PASP*, **72**, 357
 Morimoto, T., & Kurokawa, H. 2003, *PASJ*, **55**, 503
 Morimoto, T., Kurokawa, H., Shibata, K., & Ishii, T. T. 2010, *PASJ*, **62**, 939
 Newton, H. W. 1935, *MNRAS*, **95**, 650
 Okamoto, T. J., Nakai, H., Keiyama, A., et al. 2004, *ApJ*, **608**, 1124
 Oliver, R., & Ballester, J. L. 2002, *SoPh*, **206**, 45
 Parenti, S. 2014, *LRSP*, **11**, 1
 Pesnell, W. D., Thompson, B. J., & Chamberlin, P. C. 2012, *SoPh*, **275**, 3
 Pintér, B., Jain, R., & Isobe, H. 2008, *ApJ*, **680**, 1560
 Ramsey, H. E., & Smith, S. F. 1966, *AJ*, **71**, 197
 Savitzky, A., & Golay, M. 1964, *AnaCh*, **36**, 1627
 Schrijver, C. J., & De Rosa, M. L. 2003, *SoPh*, **212**, 165
 Shen, C., Wang, Y., Wang, S., et al. 2012, *NatPh*, **8**, 923
 Shen, Y., Ichimoto, K., Ishii, T. T., et al. 2014, *ApJ*, **786**, 151
 Shen, Y., & Liu, Y. 2012a, *ApJ*, **753**, 53
 Shen, Y., & Liu, Y. 2012b, *ApJ*, **754**, 7
 Shen, Y., & Liu, Y. 2012c, *ApJL*, **752**, L23
 Shen, Y., Liu, Y., & Su, J. 2012d, *ApJ*, **750**, 12
 Shen, Y., Liu, Y., Su, J., & Deng, Y. 2012e, *ApJ*, **754**, 164
 Shen, Y., Liu, Y., Su, J., et al. 2013a, *ApJ*, **773**, L33
 Shen, Y., Liu, Y., Su, J., et al. 2013b, *SoPh*, **288**, 585
 Shen, Y.-D., Liu, Y., & Liu, R. 2011, *RAA*, **11**, 594
 Sripathi, S., Balachandran, N., Veenadhari, B., Singh, R., & Emperumal, K. 2013, *JGR*, **118**, 2648
 Srivastava, A. K., & Goossens, M. 2013, *ApJ*, **777**, 17
 Tan, B., & Tan, C. 2012, *ApJ*, **749**, 28
 Thompson, B. J., & Myers, D. C. 2009, *ApJS*, **183**, 225
 Tripathi, D., Isobe, H., & Jain, R. 2009, *SSRv*, **149**, 283
 Tziotziou, K. 2007, in ASP Conf. Ser. 368, *The Physics of Chromospheric Plasmas*, ed. P. Heinzel, I. Dorotović, & R. J. Rutten (San Francisco, CA: ASP), **217**
 Uchida, Y. 1968, *SoPh*, **4**, 30
 Uchida, Y. 1970, *PASJ*, **22**, 341
 Ueno, S., Nagata, S., Kitai, R., & Kurokawa, H. 2004, in ASP Conf. Ser. 325, *The Solar-B Mission and the Forefront of Solar Physics*, ed. T. Sakurai & T. Sekii (San Francisco, CA: ASP), **319**
 Vršnak, B., Veronig, A. M., Thalmann, J. K., & Žic, T. 2007, *A&A*, **471**, 295
 Vršnak, B., Warmuth, A., Brajša, R., & Hanslmeier, A. 2002, *A&A*, **394**, 299
 Wang, J., & Ji, H. 2013, *ScChD*, **56**, 1091
 Warmuth, A., Vršnak, B., Magdalenic, J., Hanslmeier, A., & Otruba, W. 2004, *A&A*, **418**, 1117
 Wills-Davey, M. J. 2006, *ApJ*, **645**, 757
 Xue, Z., Yan, X., Qu, Z., & Zhao, L. 2014, *NewA*, **26**, 23
 Xue, Z. K., Qu, Z. Q., Yan, X. L., Zhao, L., & Ma, L. 2013, *A&A*, **556**, A152
 Yang, L., Zhang, J., Liu, W., Li, T., & Shen, Y. 2013, *ApJ*, **775**, 39
 Yuan, D., Shen, Y., Liu, Y., et al. 2013, *A&A*, **554**, A144
 Zhang, Q. M., Chen, P. F., Xia, C., & Keppens, R. 2012, *A&A*, **542**, A52
 Zhang, Q. M., Chen, P. F., Xia, C., Keppens, R., & Ji, H. S. 2013, *A&A*, **554**, A124
 Zheng, R.-S., Jiang, Y.-C., Yang, J.-Y., et al. 2013, *MNRAS*, **431**, 1359